J. Fluid Mech. (1992), *vol.* 236, *pp.* 445–460
Printed in Great Britain

A numerical study of vortex shedding from flat plates with square leading and trailing edges

By YUJI OHYA[1], YASUHARU NAKAMURA[1], SHIGEHIRA OZONO[1], HIDEKI TSURUTA[1]† AND RYUZO NAKAYAMA[2]

[1] Research Institute for Applied Mechanics, Kyushu University, Kasuga 816, Japan
[2] National Technical College of Kitakyushu, Kitakyushu 803, Japan

(Received 31 August 1990 and in revised form 4 March 1991)

This paper describes a numerical study of the flow around flat plates with square leading and trailing edges on the basis of a finite-difference analysis of the two-dimensional Navier–Stokes equations. The chord-to-thickness ratio of a plate, d/h, ranges from 3 to 9 and the value of the Reynolds number based on the plate's thickness is constant and equal to 10^3. The numerical computation confirms the finding obtained in our previous experiments that vortex shedding from flat plates with square leading and trailing edges is caused by the impinging-shear-layer instability. In particular, the Strouhal number based on the plate's chord increases stepwise with increasing d/h in agreement with the experiment. Numerical analyses also provide some crucial information on the complicated vortical flow occurring near the trailing edge in conjunction with the vortex shedding mechanism. Finally, the mechanism of the impinging-shear-layer instability is discussed in the light of the experimental and numerical findings.

1. Introduction

There have been only a few studies of vortex shedding from elongated bluff cylinders (e.g. Parker & Welsh 1983; Stokes & Welsh 1986; Nakamura & Nakashima 1986; Okajima 1988), in spite of its considerable importance in practical applications associated with many problems such as flow-induced structural or acoustic vibrations.

Our previous experiments (Nakamura, Ohya & Tsuruta 1991) on vortex shedding from flat plates with square leading and trailing edges having chord-to-thickness ratios $d/h = 3$–16, where d is chord and h is thickness, at Reynolds numbers $(1\text{–}3) \times 10^3$, showed that vortex shedding from flat plates is characterized by the impinging-shear-layer instability where the separated shear layer becomes unstable in the presence of a sharp trailing-edge corner. The Strouhal number S_d based on the plate's chord was approximately constant and equal to 0.6 for $d/h = 3$–5. With further increase in d/h up to 15, it increased stepwise to values that were approximately equal to integral multiples of 0.6. The number of vortices that were formed on the plate's side increased in correspondence with the stepwise increase in the Strouhal number.

Although our experimental findings have shed new light on the nature of vortex shedding from flat plates, a number of flow features still remain to be understood

† Present address: Mitsubishi Heavy Industries Ltd., Nagasaki-Shipyard, Nagasaki 850-91, Japan.

more clearly and extensively. These include the separated and reattaching flow on the plate's side controlled by the impinging-shear-layer instability, vortex interactions occurring near the trailing-edge corners in conjunction with the above instability, and the structure of the vortical wake as a result of these interactions. Incidentally, the shear layers separating from the leading edges in our experiment were fully turbulent with transition occurring about $1h$ downstream of the leading edges.

For a variety of two-dimensional separated and reattaching flows past elongated bodies such as blunt plates (Kiya & Sasaki 1983, 1985; Kiya 1987; Cherry, Hillier & Latour 1984) and backward-facing steps (Troutt, Scheelke & Norman 1984; Roos & Kegelman 1986), it has been widely recognized that flows at high Reynolds numbers with separation and reattachment are characterized by strong rolled-up vortices formed in a separated turbulent shear layer. The frequencies of these vortices, though not very well defined owing to the inherent turbulent fluctuations, decrease as they go downstream until becoming approximately constant after the mean reattachment point is passed. The Strouhal number based on the mean reattachment length for the constant frequency is around 0.7 (Cherry *et al.* 1984). It has been considered that those rolled-up vortices are generated by the Kelvin–Helmholtz instability. In our experiment on flat plates with square leading and trailing edges (Nakamura *et al.* 1991), we also observed such small rolled-up vortices in the turbulent separated shear layers, but we have suggested (Nakamura & Nakashima 1986; Nakamura *et al.* 1991) that their final stage with an approximately constant Strouhal number is generated by the impinging-shear-layer instability. An important question arises, therefore, as to a possible relation between these two instabilities, i.e. the impinging-shear-layer instability and the Kelvin–Helmholtz instability that precedes it.

In the present paper we have analysed unsteady viscous flows around flat plates with $d/h = 3$–9 at a Reynolds number of 10^3. The two-dimensional unsteady Navier–Stokes equations were solved directly by a finite-difference method in a generalized coordinate system using a third-order upwind scheme for the convection terms. Numerical analysis can shed light on the details of the flow that have not been explored in the experiment. The computed results are analysed and compared with those of our previous experiment, and the mechanism of the impinging-shear-layer instability is discussed in the light of the experimental and numerical findings.

2. Basic equations and numerical methods

Let us consider a uniform flow past a flat plate with square leading and trailing edges at zero incidence, as shown in figure 1. The two-dimensional Navier–Stokes and continuity equations for unsteady incompressible viscous flow can be written in dimensionless form as

$$\frac{\partial u}{\partial x}+\frac{\partial v}{\partial y}=0, \tag{1}$$

$$\frac{\partial u}{\partial t}+u\frac{\partial u}{\partial x}+v\frac{\partial u}{\partial y}=-\frac{\partial p}{\partial x}+\frac{1}{Re}\left(\frac{\partial^2 u}{\partial x^2}+\frac{\partial^2 u}{\partial y^2}\right), \tag{2}$$

$$\frac{\partial v}{\partial t}+u\frac{\partial v}{\partial x}+v\frac{\partial v}{\partial y}=-\frac{\partial p}{\partial y}+\frac{1}{Re}\left(\frac{\partial^2 v}{\partial x^2}+\frac{\partial^2 v}{\partial y^2}\right), \tag{3}$$

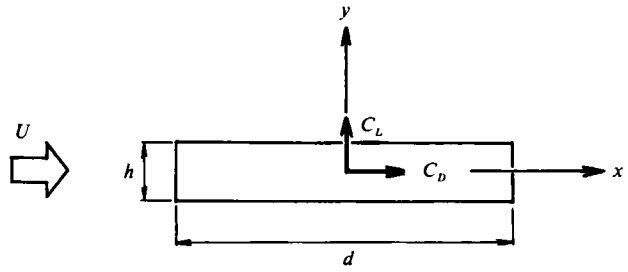

FIGURE 1. Schematic of flow configuration, coordinate system and fluid force coefficients.

with the following dimensionless variables:

$$x = \frac{x^*}{h}, \quad y = \frac{y^*}{h}, \quad t = \frac{t^*U}{h}, \quad p = \frac{p^*}{\rho U^2}, \quad u = \frac{u^*}{U}, \quad v = \frac{v^*}{U}, \quad Re = \frac{Uh}{\nu},$$

where (u, v) are the velocity components in the x- and y-directions, respectively, in a Cartesian reference frame, p the pressure, ν the kinematic viscosity, U the upstream velocity and Re the Reynolds number.

In the pressure–velocity formulation, (2) and (3) are solved in conjunction with a Poisson equation for the pressure which is obtained by taking the divergence of (2) and (3). Hence, the governing equations in vector form to be solved numerically in this approach can be summarized as follows:

$$\frac{\partial \boldsymbol{v}}{\partial t} + (\boldsymbol{v}\cdot\nabla)\,\boldsymbol{v} = -\nabla p + \frac{1}{Re}\nabla^2 \boldsymbol{v}, \tag{4}$$

$$\nabla^2 p = -\nabla\cdot(\boldsymbol{v}\cdot\nabla)\,\boldsymbol{v} + \frac{1}{Re}\nabla^2(\nabla\cdot\boldsymbol{v}) - \frac{\partial}{\partial t}(\nabla\cdot\boldsymbol{v}), \tag{5}$$

subject to the initial and boundary conditions.

The numerical analysis technique for solving (4) and (5) is based on the MAC method due to Harlow & Welch (1965). We first approximate the time derivatives of (5) with the forward difference:

$$\nabla^2 p^{n+1} = -\nabla\cdot[(\boldsymbol{v}^n\cdot\nabla)\,\boldsymbol{v}^n] + \frac{D^n}{\Delta t} + \frac{1}{Re}\nabla^2 D^n, \tag{6}$$

where $D = \nabla\cdot\boldsymbol{v}$, Δt is the time increment and n denotes the integration time step $n = t/\Delta t$. In (6), $D^n/\Delta t$ may be interpreted as a discretization of $-\partial D/\partial t$ with $D^{n+1} = 0$. Thus the converged pressure solution resulting from (6) is such as to cause the discrete form of the continuity equation to be satisfied at time level $n+1$.

The Euler implicit scheme is used for the time integration of (4):

$$\frac{\boldsymbol{v}^{n+1} - \boldsymbol{v}^n}{\Delta t} + (\boldsymbol{v}^n\cdot\nabla)\,\boldsymbol{v}^{n+1} = -\nabla p + \frac{1}{Re}\nabla^2 \boldsymbol{v}^{n+1}. \tag{7}$$

Here, the convection term is linearized as follows:

$$(\boldsymbol{v}\cdot\nabla)\,\boldsymbol{v} = (\boldsymbol{v}^{n+1}\cdot\nabla)\,\boldsymbol{v}^{n+1} \approx (\boldsymbol{v}^n\cdot\nabla)\,\boldsymbol{v}^{n+1}. \tag{8}$$

If $\boldsymbol{v}$ is given at a time step n, the Poisson equation (6) can be solved to obtain p; then by substituting these values into (7), $\boldsymbol{v}$ at the next time step $(n+1)$ is calculated.

In order to simulate the flow around a body of arbitrary shape with high accuracy,

it is convenient to use body-fitted coordinates through coordinate transformations in the governing equations. The coordinate transformation is defined by

$$x = x(\xi, \eta), \quad y = y(\xi, \eta), \tag{9}$$

where (x, y) denotes the original physical plane and (ξ, η) denotes the computational plane.

By using (9), equations (4) and (5) are transformed as follows:

$$u_t + \left(\frac{uy_\eta - vx_\eta}{J}\right)u_\xi + \left(\frac{vx_\xi - uy_\xi}{J}\right)u_\eta = -\frac{y_\eta p_\xi - y_\xi p_\eta}{J} + \frac{1}{Re}\tilde{\Delta}u, \tag{10}$$

$$v_t + \left(\frac{uy_\eta - vx_\eta}{J}\right)v_\xi + \left(\frac{vx_\xi - uy_\xi}{J}\right)v_\eta = -\frac{x_\xi p_\eta - x_\eta p_\xi}{J} + \frac{1}{Re}\tilde{\Delta}v, \tag{11}$$

$$\tilde{\Delta}p = -\frac{(y_\eta u_\xi - y_\xi u_\eta)^2 + 2(x_\xi u_\eta - x_\eta u_\xi)(y_\eta v_\xi - y_\xi v_\eta) + (x_\xi v_\eta - x_\eta v_\xi)^2}{J^2} + \frac{y_\eta u_\xi - y_\xi u_\eta + x_\xi v_\eta - x_\eta v_\xi}{J\,\Delta t}, \tag{12}$$

where the operator $\tilde{\Delta}$ is defined by

$$\tilde{\Delta}A = \frac{\alpha A_{\xi\xi} - 2\beta A_{\xi\eta} + \gamma A_{\eta\eta}}{J^2} + \frac{(\alpha x_{\xi\xi} - 2\beta x_{\xi\eta} + y x_{\eta\eta})(y_\xi A_\eta - y_\eta A_\xi) + (a y_{\xi\xi} - 2\beta y_{\xi\eta} + \gamma y_{\eta\eta})(x_\eta A_\xi - x_\xi A_\eta)}{J^3}, \tag{13}$$

and

$$J = x_\xi y_\eta - x_\eta y_\xi, \quad \alpha = x_\eta^2 + y_\eta^2, \quad \beta = x_\xi x_\eta + y_\xi y_\eta, \quad \gamma = x_\xi^2 + y_\xi^2. \tag{14}$$

The boundary conditions are given as follows:

(i) On the body where $\eta = 0$, the fluid velocity is zero, i.e. $u = 0, v = 0$. The pressure on the body is determined by substituting $u = 0$ and $v = 0$ into (10) and (11):

$$p_\eta = \frac{1}{Re}(x_\eta \tilde{\Delta}u + y_\eta \tilde{\Delta}v). \tag{15}$$

(ii) On the remote boundary where $\eta = \eta_{\max}$, the flow is assumed to be uniform, i.e. $u = 1, v = 0$. The pressure is determined by extrapolation. The initial conditions are given as $u = 0, v = 0, p = 0$.

All the spatial derivatives of (10)–(12) except those of the convection terms are approximated by central finite difference. For the convection terms, a third-order upwind scheme proposed by Kawamura & Kuwahara (1984) is used, i.e.

$$\left(f\frac{\partial u}{\partial \xi}\right)_{i,j} = f_{i,j}\frac{-u_{i+2,j} + 8(u_{i+1,j} - u_{i-1,j}) + u_{i-2,j}}{12\Delta\xi} + |f_{i,j}|\frac{u_{i+2,j} - 4u_{i+1,j} + 6u_{i,j} - 4u_{i-1,j} + u_{i-2,j}}{4\Delta\xi}, \tag{16}$$

where f is an arbitrary function, (i, j) denotes the grid point, and $\Delta\xi$ is the grid scale. The leading error of this scheme is estimated to be

$$(\Delta\xi)^3 |f| \frac{\partial^4 u}{\partial \xi^4},$$

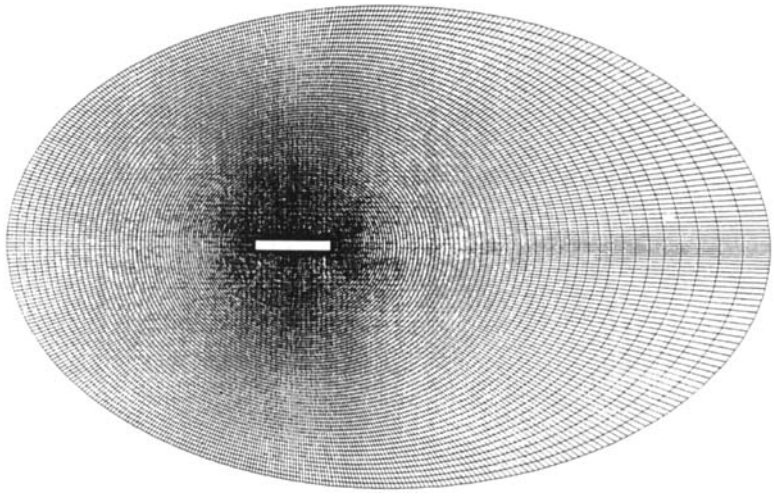

FIGURE 2. Typical computational grid (a flat plate with $d/h = 8$, 453×81).

which is only slightly dissipative.

Thus the finite-difference equations are obtained by discretizing (10)–(12) written in a generalized coordinate system (ξ, η). They are solved using the successive over-relaxation method. The regular mesh system is employed to evaluate u, v, p at the mesh points. The time increment Δt is $(1 \text{ or } 2) \times 10^{-3}$.

In order to generate a grid system, an elliptic mapping method proposed by Thames *et al.* (1977) is used; the curvilinear coordinates are generated as contours of the solutions of two Poisson equations:

$$\xi_{xx} + \xi_{yy} = P, \quad \eta_{xx} + \eta_{yy} = Q. \tag{17}$$

Adjusting Q, it is possible to concentrate grid points near the cylinder surface. Figure 2 shows a typical grid used in the present calculation. For a flat plate with a long chord, it is necessary to set a large number of grid lines in the ξ-direction to keep the grid resolution. The outer boundary is set at about $20h$–$50h$ upstream and $50h$–$110h$ downstream from the centre of the plate and about $25h$–$50h$ away in the vertical direction. In the following calculations, various grid sizes are employed for different flat plates, as shown in table 1. All the numerical calculations in this work were carried out on a system consisting of FACOM M-780/20 and FACOM VP-200 computers at Kyushu University. The typical CPU time required increased with d/h of the flat plate; for example, approximately 2 hours for $d/h = 3$ and approximately 24 hours for $d/h = 9$.

3. Numerical results

When triggering vortex shedding from the flat plates, no asymmetry was added artificially. Initially, separation bubbles were formed symmetrically on both sides of a plate, while a pair of attached eddies was formed at the rear. The separation bubbles increased in length with increasing time until reaching the rear edges, and then began to interact with the attached eddies. At this stage, asymmetry of the flow appeared, which led to regular or irregular asymmetric vortex shedding. It took about 80 non-dimensional times for stationary vortex shedding to be established.

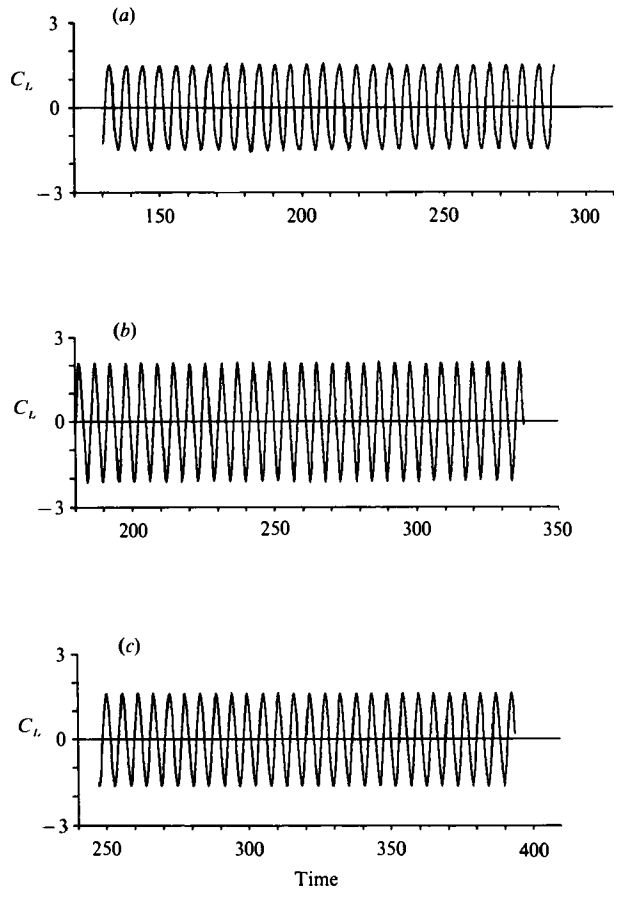

FIGURE 3. Time histories of lift coefficient C_L for flat plates with (*a*) $d/h = 3$; (*b*) 6; (*c*) 9.

3.1. *Flat plates with* $d/h = 3$, 6 *and* 9

3.1.1. *Time history of lift coefficient*

Figure 3(*a–c*) shows time histories of the lift coefficient C_L for flat plates with $d/h = 3, 6$ and 9, respectively, at $Re = 10^3$. All the figures show a regular fluctuation with a constant amplitude. It is clear that there is periodic vortex shedding from the flat plates. To calculate the Strouhal number S_d, which is based on the plate's chord, the power spectra of C_L fluctuations were obtained by an FFT analysis. As is shown in table 1, the computed values of S_d for flat plates with $d/h = 3$, 6 and 9 are 0.52, 1.10 and 1.63, respectively. It should be noted that the ratio of these values is nearly 1:2:3. Table 1 also includes the computed results for the mean and r.m.s. lift coefficients, the mean drag coefficient, and the Strouhal number based on the thickness h.

3.1.2. *Flow over the plate's side*

The flow around a long flat plate with square leading and trailing edges is characterized by a separated and reattaching flow phenomenon. Figures 4, 5 and 6 show time sequences of (i) streamlines and (ii) vorticity contours covering one cycle of vortex shedding for a plate with $d/h = 6$ (figure 5), and a half-cycle for plates with $d/h = 3$ (figure 4) and $d/h = 9$ (figure 6). As can be seen in figure 5(*a–d*), the shear layer separating from the leading edge reattaches to the plate's side and forms a

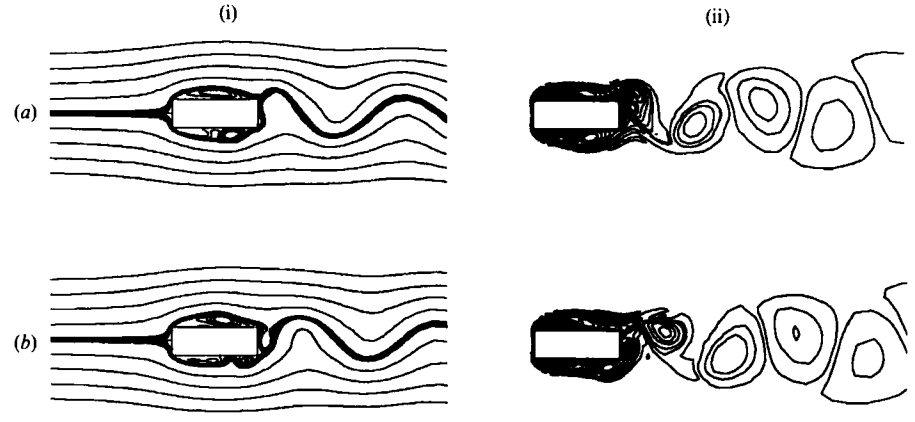

FIGURE 4. Time sequence of flow pattern around a flat plate with $d/h = 3$ covering half a shedding cycle. (i) Streamlines; (ii) vorticity contours. (*a*) Minimum C_L; (*b*) $C_L = 0$.

d/h	Grid size	C_D	C_L	C_{Lrms}	S_h	S_d	m
3	209 × 81	1.34	0	1.06	0.174	0.52	1
4	261 × 81	1.44	0	1.19	0.150	0.60	1
		1.29	−0.35	1.18	0.150	0.60	1
5	313 × 81	1.04	0	—	0.117	0.59	1
6	365 × 81	1.26	0	1.48	0.183	1.10	2
7	417 × 81	1.06	0	—	0.164	1.15	2
8	453 × 81	0.97	0	—	0.137	1.10	2
		1.02	0	0.76	0.181	1.45	3
9	505 × 81	0.90	0	1.12	0.181	1.63	3

TABLE 1. Grid sizes and computational results of characteristic parameters of flat plates at $Re = 10^3$: $C_D = D/(0.5\rho U^2 h)$, drag coefficient; $C_L = L/(0.5\rho U^2 h)$, lift coefficient; C_{Lrms}, r.m.s. of fluctuating lift coefficient; D, drag force; L, lift force; ρ, fluid density; S_d, Strouhal number based on chord; S_h, Strouhal number based on height; m, number of vortices along the side

separation bubble. The bubble oscillates in length at a regular frequency which is equal to the vortex shedding frequency. The bubble increases steadily in length until the bounding shear layer halfway along the bubble deflects towards the surface and reattaches. This splits the bubble into two with the upstream section beginning to grow again and the downstream section moving along the plate's side as a discrete vortex.

It is worth noting from figure 4(*a*) that during the vortex shedding just one vortex (a separation bubble) is formed on the plate's side for a flat plate with $d/h = 3$. In other words, the spacing of vortices on the side is just equal to the plate's chord. Similarly, two vortices are formed on the side for a flat plate with $d/h = 6$, and three vortices, for $d/h = 9$. Thus, the number of vortices that are formed on the plate's side for these three plates corresponds to the ratio of the values of the Strouhal number S_d, i.e. 1:2:3.

3.1.3. *Trailing-edge flow*

Let us now observe the flow near the trailing edge. The vortex formed on the plate's side is hereafter called the L vortex for brevity. Figures 4–6 show that before the L vortex approaches the trailing edge, the reattached boundary layer separates

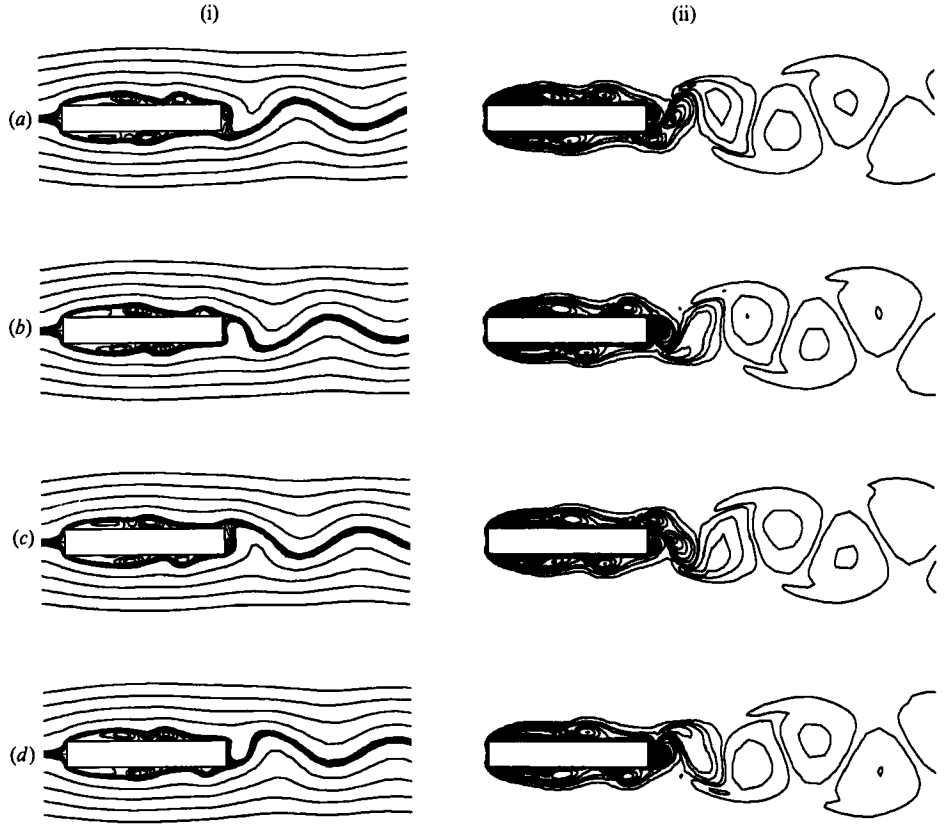

FIGURE 5. Time sequence of flow pattern around a flat plate with $d/h = 6$ covering one shedding cycle. (i) Streamlines; (ii) vorticity contours. (*a*) Maximum C_L; (*b*) $C_L = 0$; (*c*) minimum C_L; (*d*) $C_L = 0$.

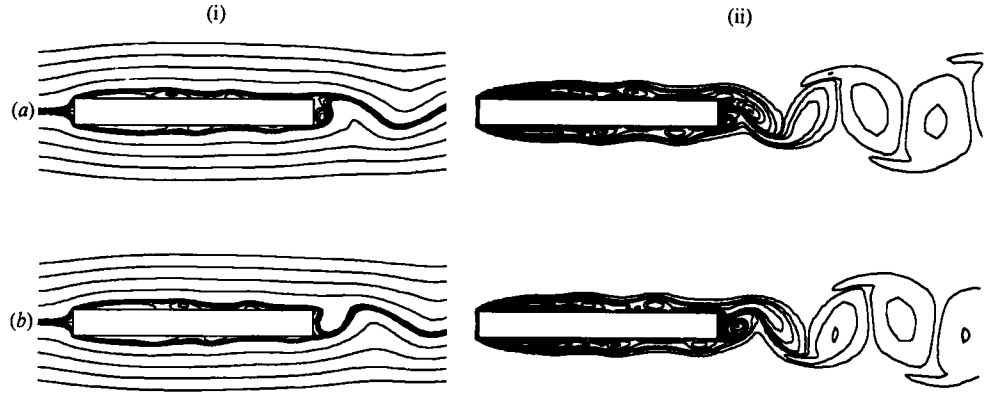

FIGURE 6. Time sequence of flow pattern around a flat plate with $d/h = 9$ covering half a shedding cycle. (i) Streamlines; (ii) vorticity contours. (*a*) Minimum C_L; (*b*) $C_L = 0$.

again at the trailing edge, thus forming a new growing vortex, which is hereafter called the T vortex. This T vortex interacts regularly with the oncoming L vortex, and they are shed in a pair in the downstream wake. (Incidentally, we do not think that their interaction is what is called 'merging'. Figures 5(*c*) and 5(*d*) suggest that they are still separate during downstream convection. It appears that the T vortex

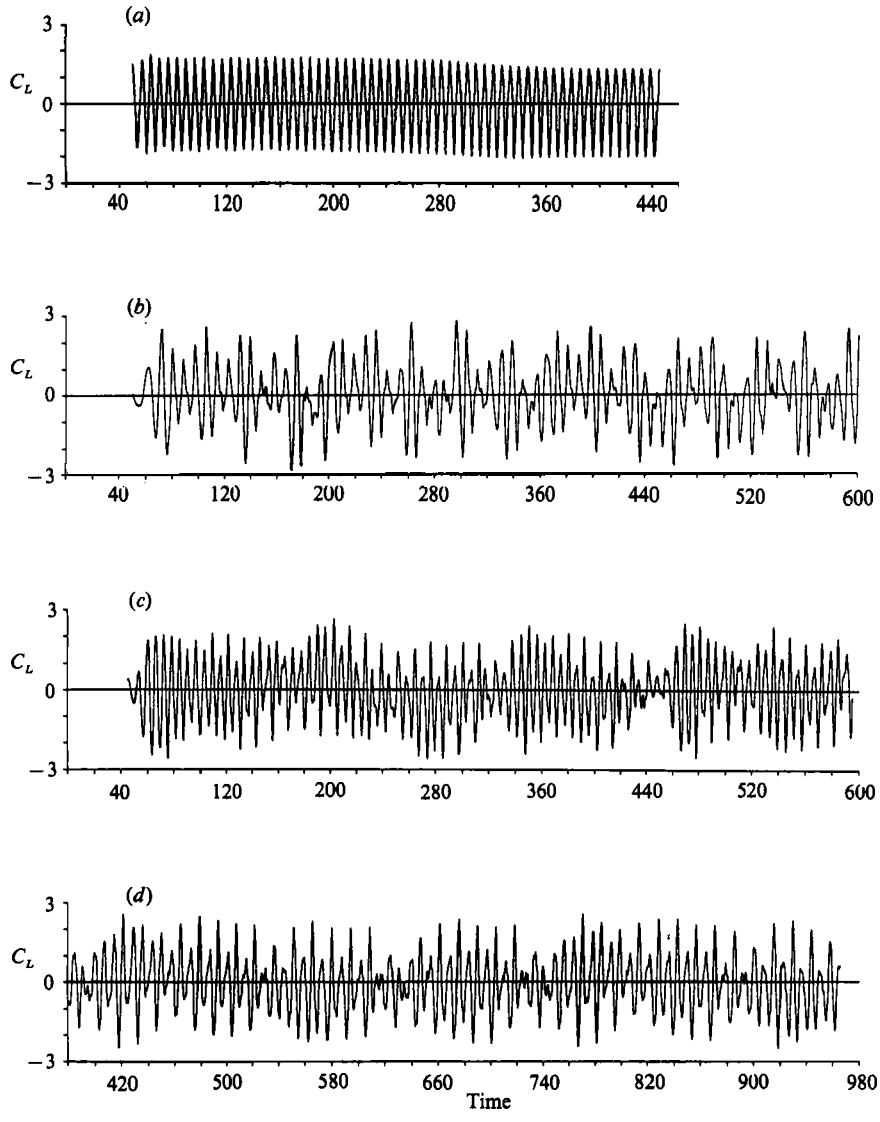

FIGURE 7. Time histories of lift coefficient C_L for flat plates with (*a*) $d/h = 4$; (*b*) 5; (*c*) 7; (*d*) 8.

is more rapidly diffused than the L vortex in this case.) The interaction between the two vortices occurs alternately at the upper and lower trailing-edge corners. Thus, a regular vortex street develops in the downstream wake (see the flow patterns depicted by vorticity contours in figures 4–6), thereby producing the regular variations of C_L shown in figure 3.

3.2. *Flat plates with* $d/h = 4$, 5, 7, *and* 8

3.2.1. *Time history of lift coefficient*

Figure 7 (*a–d*) shows time histories of C_L for flat plates with $d/h = 4$, 5, 7 and 8, respectively, which contrast to those for $d/h = 3$, 6 and 9 (figure 3). The C_L variations for $d/h = 5$, 7 and 8 show markedly irregular fluctuations. However, the power spectra of the C_L fluctuations reveal that they still have a dominant frequency. For example, figure 8 shows that a dominant peak can be seen in the power spectrum for

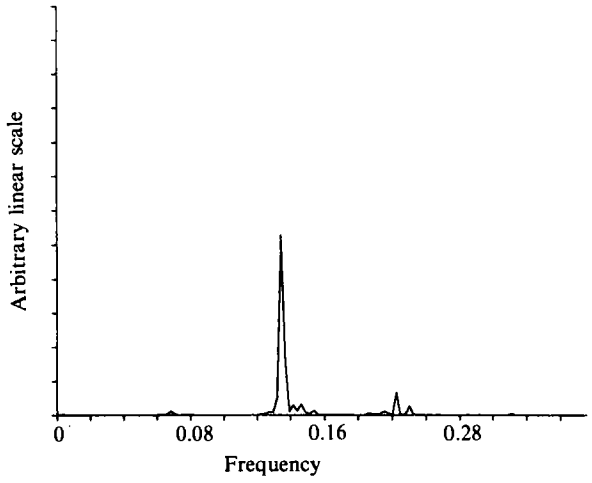

FIGURE 8. Power spectrum of C_L fluctuation for a flat plate with $d/h = 8$.

a flat plate with $d/h = 8$. The case with $d/h = 4$ is different, however: as can be seen in figure 7 (a), a regular time variation of C_L appears at first (having zero time-mean value) and is replaced by another variation that still has a regular oscillation with the same frequency and amplitude but with a non-zero time-mean value.

The values of the Strouhal number S_d for flat plates with $d/h = 4$ and 5 are 0.60 and 0.59, respectively. It is interesting that these values are nearly equal to that for $d/h = 3$ of 0.52. Similarly, the computed values for flat plates with $d/h = 7$ and 8 are 1.15 and 1.10, respectively, which are again nearly equal to that for $d/h = 6$ of 1.10.

3.2.2. *Trailing-edge flow*

In order to investigate the cause of the random modulations in C_L, we will observe the trailing-edge flow in detail for a flat plate with $d/h = 8$. Figure 9 shows a time sequence of vorticity contours covering almost two shedding cycles with a positive time-mean value of C_L (e.g. $t = 400$–460 or 760–820 in figure 7d).

We notice first that during the two cycles of shedding shown, L vortices on the side are shed periodically at the fundamental frequency. However, the interaction of L and T vortices at the trailing edge adds further periodic and/or irregular perturbations. For example, comparing the flow patterns in figure 9 (a, d, h), where a similar phase of shedding is observed on the side, we see that the downstream flow developments shown in figures 9 (a) and 9 (h) are similar, while that shown in figure 9 (d) is different from the other two, particularly near the trailing edge. This feature corresponds to the time history of C_L shown in figure 7 (d), where large-amplitude fluctuations repeat at almost every two cycles of oscillation.

We shall now consider the interaction between L and T vortices at the trailing edge in more detail. At the lower trailing edge, the interaction is basically the same as that shown in figure 5, namely, L and T vortices are shed in a pair from the trailing edge (see figures 9c–9e, for example). However, the spacing between the vortex pair is relatively large so that the vorticity contours are much elongated.

By contrast, the interaction at the upper trailing edge is different for two successive cycles of shedding. During one cycle of shedding (figures 9a–9d) L and T vortices are shed separately from the trailing edge. During the next cycle of shedding (figures 9e–9h), however, the normal interaction resumes, where L and T vortices are shed in a pair from the trailing edge.

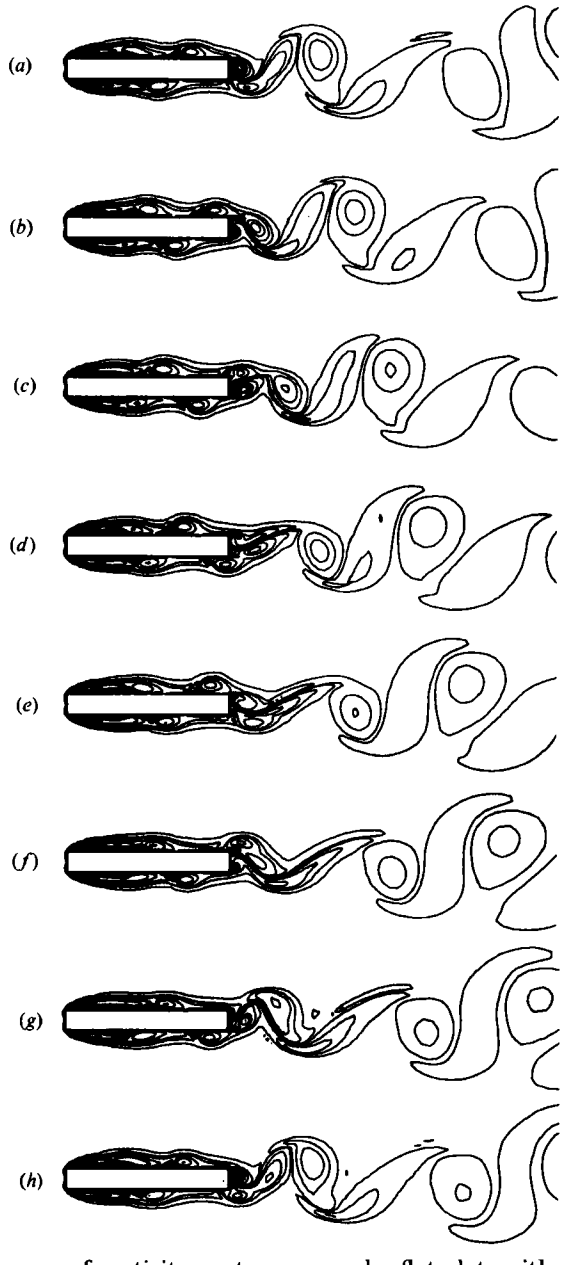

FIGURE 9. Time sequence of vorticity contours around a flat plate with $d/h = 8$ covering two shedding cycles.

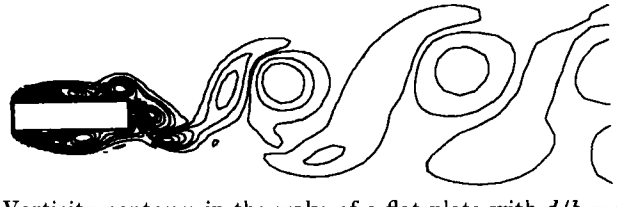

FIGURE 10. Vorticity contours in the wake of a flat plate with $d/h = 4$ at $C_L = 0$.

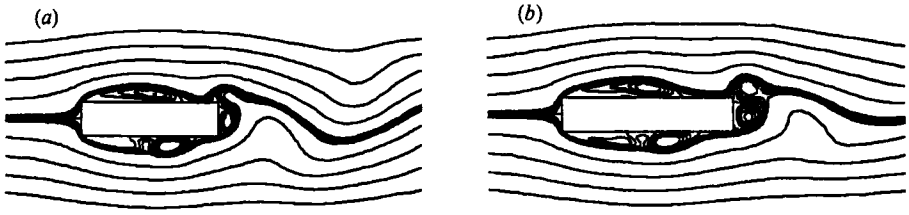

FIGURE 11. Streamlines around flat plates corresponding to minimum C_L: (*a*) $d/h = 4$ ($t = 92.9$); (*b*) 5 ($t = 572.0$).

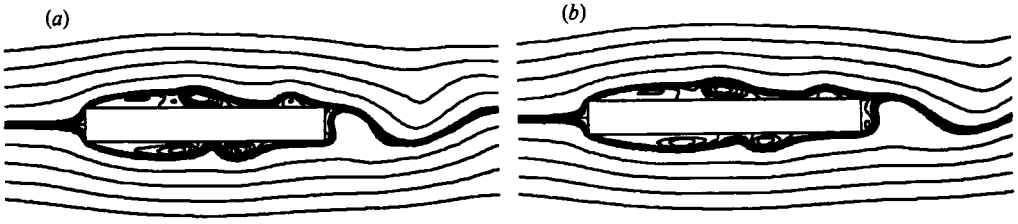

FIGURE 12. Streamlines around flat plates corresponding to $C_L = 0$: (*a*) $d/h = 7$ ($t = 104.6$); (*b*) 8 ($t = 439.0$).

In addition to the rather periodic perturbations mentioned above, the interaction can also introduce irregular fluctuations into the flow field. The source of the irregular fluctuations can perhaps be attributed to the phasing of shedding of the L and T vortices at the upper and lower trailing-edge corners. In the time history of C_L shown in figure 7(*d*), two different phases of the lift fluctuation, where the mean values are positive and negative, respectively, repeat one after another at irregular intervals. Broadly speaking, the mirror-image of the flow patterns shown in figure 9 should appear in the time intervals, for example, $t = 540$–600 or 900–960, where the mean C_L value is negative.

The time variation of C_L shown in figure 7(*a*) for a flat plate with $d/h = 4$ suggests that the flow has gradually shifted from a symmetric pattern to an asymmetric one, both having the same frequency of oscillation. The new asymmetric flow pattern is shown in figure 10. It is interesting that a flat plate with a symmetric shape placed in a uniform flow at zero attack angle can generate such an asymmetric flow pattern. This may also be caused by a slight asymmetry of interactions between L and T vortices at the upper and lower trailing-edge corners. In the vorticity field shown in figure 10, the spacing between the vortex pair shed from the upper side of a plate is relatively small, while for that shed from the lower side it is large. As a result, the vorticity shed from the upper trailing edge is more concentrated than that from the lower trailing edge, thus producing a negative mean lift force (figure 7*a*).

3.2.3. *Flow along the plate's side*

The flows along the side for flat plates with different values of d/h but with approximately the same values of the Strouhal number S_d are similar, although the interactions between vortices at the trailing edges can produce some variations in the subsequent flow development. Thus, figures 11(*a*) and 11(*b*) for flat plates with $d/h = 4$ and 5, respectively, can be compared with figure 4(*a*) for a flat plate with $d/h = 3$. All of them indicate approximately the same phase of vortex shedding. Similarly, figures 12(*a*) and 12(*b*) for flat plates with $d/h = 7$ and 8, respectively, can be compared with figure 5(*b*) for a flat plate with $d/h = 6$.

4. Impinging-shear-layer instability

4.1. *Comparison with experiment*

As was mentioned earlier, our previous experiment on flat plates at $Re = (1\text{–}3) \times 10^3$ (Nakamura *et al.* 1991) showed that vortex shedding from flat plates is characterized by the impinging-shear-layer instability. The results of these experimental measurements of the Strouhal number at $Re = 10^3$ are shown plotted against the chord-to-thickness ratio d/h in figure 13. The Strouhal number S_d increases stepwise to values that are approximately equal to integral multiples of 0.6. Each branch of nearly constant S_d is given an integer m.

The computed values of S_d in the present numerical study are also shown in figure 13. They again show a stepwise increase with increasing d/h in agreement with the experiment. Thus, the present numerical analysis has confirmed that vortex shedding from flat plates can be caused by the impinging-shear-layer instability, where the shear layer separating from the leading-edge corner becomes unstable in the presence of a sharp trailing-edge corner. Flat plates with $d/h = 3\text{–}5$ are grouped into the first branch of vortex shedding $m = 1$; similarly, flat plates with $d/h = 6\text{–}8$ are grouped into the second branch $m = 2$, and a flat plate with $d/h = 9$ in the third branch $m = 3$. There is close similarity in the flow for each branch, which is characterized by the number m of vortices formed on the plate's side. Among flat plates belonging to each branch the one with smallest d/h is the most basic in the manner of vortex shedding. The numerical analysis has shown that this is because only this plate has very regular vortex shedding, while irregularities in vortex shedding emerge to increase with increasing d/h. In parallel with the experiment, the values of S_d for the basic plates lie on a straight line passing through the origin.

S_d often had two values at the stepwise jump for the same d/h in our previous experiments. In the numerical analysis, we also obtained two values of S_d for a flat plate with $d/h = 8$, the low and high values corresponding to the branches of $m = 2$ and $m = 3$, respectively (figure 13). This will be discussed again in §5.

4.2. *Mechanism of the impinging-shear-layer instability*

A number of important conclusions on the nature of the impinging-shear-layer instability can be drawn from a careful comparison between the experiments and the numerical analysis. We should first mention essential differences in the flow conditions between the two. Our flow visualization (Nakamura *et al.* 1991) revealed that the flow around a flat plate at $Re = 10^3$ is turbulent with inherent random fluctuations, namely transition from laminar to turbulent flow occurred in the shear layer immediately after separation, i.e. about $1h$ downstream of the leading edge. The flow after separation was initially two-dimensional but three-dimensional random modulations developed when the curvature of the turbulent shear layer was reversed. On the other hand, the flow in the present numerical analysis is purely two-dimensional and laminar everywhere including the separated shear layers. Our numerical analysis has shown that the impinging-shear-layer instability can be generated in a purely two-dimensional laminar flow. The good agreement between the experiment and the numerical analysis in the S_d variation with d/h, therefore, suggests that the impinging-shear-layer instability is not essentially influenced by any transition processes and/or turbulence.

Our flow visualization on flat plates at $Re = 10^3$ also showed that the impinging-shear-layer instability was preceded by the Kelvin–Helmholtz instability. In the present numerical analysis, however, we have found no trace of a Kelvin–Helmholtz

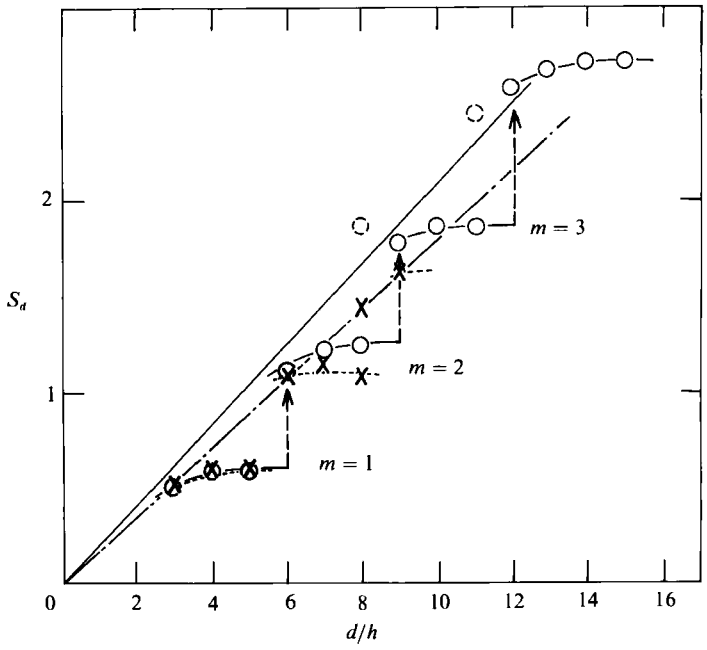

FIGURE 13. Strouhal number S_d based on the chord *vs.* chord-to-thickness ratio d/h at $Re = 10^3$: ○ ——, experimental (Nakamura *et al.* 1991); × —·—, numerical.

instability preceding the impinging-shear-layer instability. This is to be expected since the Kelvin–Helmholtz instability is a kind of free-shear-layer instability, while the presence of the trailing-edge corner is essential to the impinging-shear-layer instability. In short, the Kelvin–Helmholtz instability is not necessary to trigger the impinging-shear-layer instability.

5. Further numerical experiments on a flat plate with $d/h = 8$

During an early phase of the present investigation, we tried to obtain the response of the flow to some artificial disturbance to check the possibility of controlling the random modulation in the flow arising from the vortex interactions at the trailing edge such as described in §3.2.2. This was successful, but we found later that such random modulations can take place spontaneously without introducing any artificial disturbance into the flow.

In one such trial on a flat plate with $d/h = 8$, we found the transition in vortex shedding from $m = 2$ to $m = 3$ that was found in our previous experiment (figure 13). The plate was initially at zero incidence and was then given a small positive incidence of 0.5° for only a short time interval $t = 616$–694, and the subsequent flow development was observed.

Figure 14 (*a*) shows the time history of the lift fluctuation, where it can be seen that for $t > 1280$, the plate is experiencing very regular vortex shedding with a zero-mean C_L value. Figures 14 (*b*) and 14 (*c*) show the streaklines and the time sequence of vorticity contours, respectively, corresponding to this regular vortex shedding. It is clear from these figures that the vortex shedding belongs to the branch of $m = 3$. It is interesting to note that the value of S_d is just on the basic line plotted in figure 13.

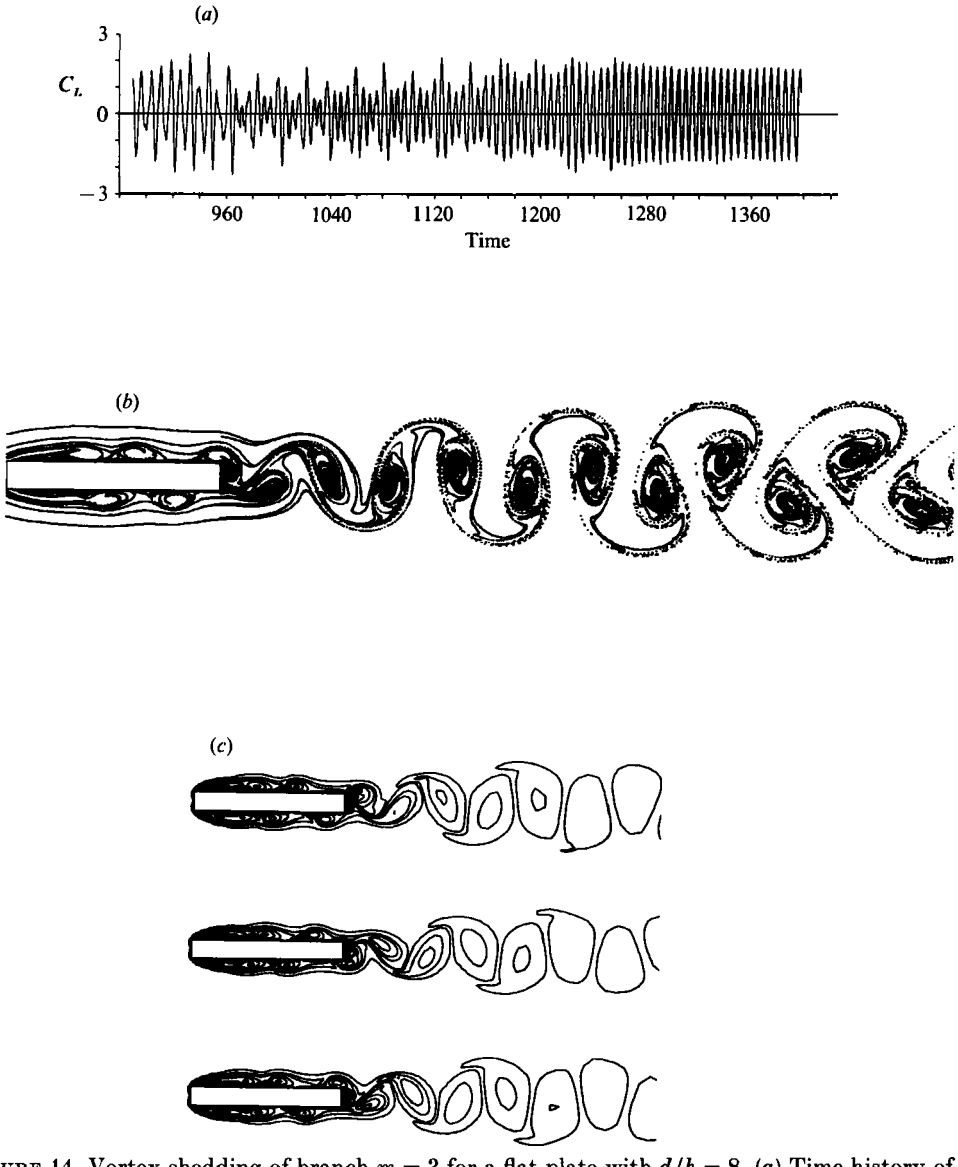

FIGURE 14. Vortex shedding of branch $m = 3$ for a flat plate with $d/h = 8$. (*a*) Time history of lift coefficient C_L; (*b*) streaklines in the wake ($t = 1397.6$); (*c*) time sequence of vorticity contours covering one shedding cycle.

6. Conclusions

Flows around flat plates with square leading and trailing edges were analysed numerically by direct integration of the Navier–Stokes equations using the finite-difference method. The chord-to-thickness ratio of a plate, d/h, ranged from 3 to 9 and the value of the Reynolds number based on the plate's thickness was constant and equal to 10^3. The main results of this study can be summarized as follows.

In agreement with our previous experiment, the numerical analysis has shown that vortex shedding from flat plates with square leading and trailing edges is characterized by the impinging-shear-layer instability, where the separated shear

layer can be unstable in the presence of a sharp trailing-edge corner. The Strouhal number S_d based on the plate's chord, shows a stepwise increase with increasing d/h. The number of vortices formed on the plate's side increases in correspondence with the stepwise increase in the Strouhal number. Among flat plates with nearly constant Strouhal numbers the one with smallest d/h is the most basic. This is because only this one has very regular vortex shedding, while irregularities in vortex shedding emerge to increase with increasing d/h. In agreement with the experiment, the numerical analysis also showed two S_d values of different branches for a flat plate with a transitional $d/h = 8$.

There are complicated interactions between the vortex being shed from upstream and that being generated at the trailing edge which control the downstream vortical flow. The source of the irregularities in the flow may be attributed to these interactions.

The impinging-shear-layer instability is not essentially influenced by any transition processes and/or turbulence. Also, the Kelvin–Helmholtz instability that often preceded it is not essential to trigger the impinging-shear-layer instability.

REFERENCES

CHERRY, N. J., HILLIER, R. & LATOUR, M. E. M. 1984 Unsteady measurements in a separated and reattaching flow. *J. Fluid Mech.* **144**, 13–46.

HARLOW, F. H. & WELCH, J. E. 1965 Numerical calculation of time-dependent viscous incompressible flow of fluid with free surface. *Phys. Fluids* **8**, 2182–2189.

KAWAMURA, T. & KUWAHARA, K. 1984 Computation of high Reynolds number flow around a circular cylinder with surface roughness. *AIAA Paper* 84-0340.

KIYA, M. 1987 Structure of flow in leading-edge separation bubbles. In *Boundary-Layer Separation* (ed. F. T. Smith & S. N. Brown), pp. 57–71. Springer.

KIYA, M. & SASAKI, K. 1983 Structure of a turbulent separation bubble. *J. Fluid Mech.* **137**, 83–113.

KIYA, M. & SASAKI, K. 1985 Structure of large-scale vortices and unsteady reverse flow in the reattaching zone of a turbulent separation bubble. *J. Fluid Mech.* **154**, 463–491.

NAKAMURA, Y. & NAKASHIMA, M. 1986 Vortex excitation of prisms with elongated rectangular, H and ⊢ cross-sections. *J. Fluid Mech.* **163**, 149–169.

NAKAMURA, Y., OHYA, Y. & TSURUTA, H. 1991 Experiments on vortex shedding from flat plates with square leading and trailing edges. *J. Fluid Mech.* **222**, 437–447.

OKAJIMA, A. 1988 Numerical simulation of flow around rectangular cylinders. *Intl Colloq. on Bluff Body Aerodynamics and Its Applications. Japan J. Wind Engng* **37**, 281–290.

PARKER, R. & WELSH, M. C. 1983 Effects of sound on flow separation from blunt flat plates. *Intl J. Heat Fluid Flow* **4**, 113–127.

ROOS, F. W. & KEGELMAN, J. T. 1986 Control of coherent structures in reattaching laminar and turbulent shear layers. *AIAA J.* **24**, 1956–1963.

STOKES, A. N. & WELSH, M. C. 1986 Flow-resonant sound interaction in a duct containing a plate, II: Square leading edge. *J. Sound Vib.* **104**, 55–73.

THAMES, F. C., THOMPSON, J. F., MASTIN, C. W. & WALKER, R. L. 1977 Numerical solutions for viscous and potential flow about arbitrary two-dimensional bodies using body-fitted coordinate systems. *J. Comput. Phys.* **24**, 245–273.

TROUTT, T. R., SCHEELKE, B. & NORMAN, T. R. 1984 Organized structures in a reattaching separated flow field. *J. Fluid Mech.* **143**, 413–427.